Near Surface Microstructures Developing under Large Sliding Loads

D.A. Hughes, D.B. Dawson, J.S. Korellis, and L.I. Weingarten

The subsurface zones of copper developed during the application of large sliding loads were observed using TEM and SEM. Differences in microstructural development as a function of load and sliding velocity are assessed. The observed microstructural changes, such as the development of a dislocation substructure and a mechanically mixed layer, are used to estimate the stress and strain-state of the near surface zone during sliding. These estimates of local stress and strain were compared to the applied stresses to show that large stress concentrations develop at and below a sliding interface. Thus, the stresses which develop locally within the near surface zone can be many times larger than those predicted from the applied load and the friction coefficient. It is postulated that these stress concentrations arise from two sources: 1) asperity interactions and 2) local and momentary bonding between the two surfaces. These results are compared to various friction models.

Keywords:
contact mechanics, copper, deformation, dislocation structure, friction, wear, grain refinement, metals, microstructure, recrystallization, strain-hardening, tribology

1. Introduction

LOCAL deformation occurs in the subsurface zones at a sliding interface and changes the microstructure in those zones. Since the local deformation changes both the microstructure and the properties of the material in the subsurface zones, it has an effect on the friction coefficient and wear properties of the material (Ref 1). Thus, these subsurface zones have often been characterized because of their role in the friction and wear of materials (Ref 1-10). The microstructure in these regions can also provide semiquantitative measurements of the stress and strain state, temperature, and changes in chemical composition from which the mechanisms of the friction process can be inferred.

An example of copper deformed by sliding under large normal loads is used in this paper to show the available methods to extract this microstructural information. The microstructural data are then compared to microstructures which develop during large strain deformation and with available friction models, such as adhesion, asperity interaction models and the mechanics contact between smooth surfaces (e.g. Hertzian models) (Ref 11-25). These friction models predict the stress and strain state expected below a sliding contact as well as the friction coefficient.

2. Experimental Procedures

High purity OFE copper 10100 in the full hard condition was machined into friction test blocks with a 25.4 mm × 25.4 mm test surface area. The surface finish on these blocks was machined so that the last two machining cuts were less than 0.013 mm each. Surface roughness was then measured to be 0.3 μm R_q (arithmetic mean deviation of the roughness profile). The machined blocks were subsequently recrystallized at 873 K in vacuum for one hour to a grain size of 100 μm. This recrystallization step removed all machining damage from the surface before sliding.

The stress-strain plots of the recrystallized copper under quasi-static conditions for both tension and torsion are shown in Fig. 1. The yield stress in tension for this material is 30 MPa.

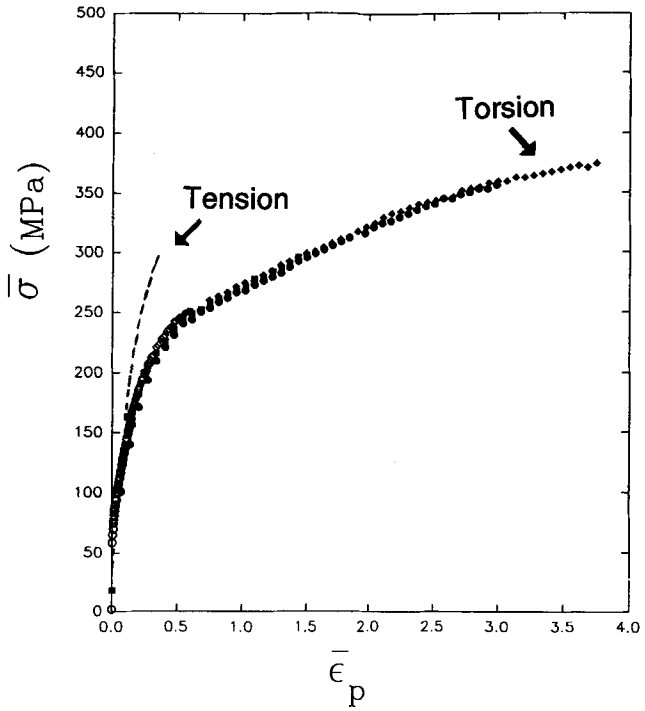

Fig. 1 True stress-true strain behavior of OFE copper during quasi-static loading for both tensile and thin-walled tube torsion deformation. The data have been plotted as $\bar{\sigma}$ and $\bar{\epsilon}$ von Mises equivalent stress and strain, respectively. Note the continued work hardening at large strains which occurs in copper. (The torsion data are courtesy of M. Miller, Cornell Univ.)

D.A. Hughes, D.B. Dawson, J.S. Korellis, and **L.I. Weingarten,** Center for Materials and Applied Mechanics, Sandia National Laboratories, Livermore CA 94550.

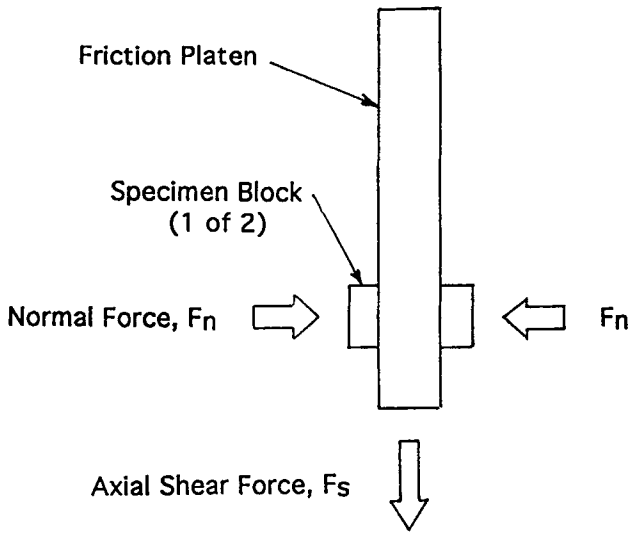

Fig. 2 A schematic drawing of the friction test apparatus to show the arrangement of the friction samples and platen.

Just before friction testing the recrystallized copper blocks were dipped for 3-5 seconds in concentrated glow brite acid. The blocks were next rinsed in water and then in isopropyl alcohol to remove the previous oxide layer. Samples were stored in the isopropyl alcohol until testing; storage did not exceed four hours. This procedure provided a very thin and more controlled oxide layer during testing.

The friction test blocks were then tested using the Sandia flat plate friction tester with a hardened 4340 steel counterface slider (platen). A schematic of this friction apparatus is shown in Fig. 2. The apparatus is described in detail in a companion paper from these proceedings (Ref 26). The apparatus connects to a servo-hydraulic test machine for control and measurement of sliding speed and normal and shear forces. This test machine is designed to test large areas and provide a known measurement of the bulk normal and shear stresses as well as the evolving global friction coefficient. The normal pressure, sliding speeds, and sliding length for the copper samples are shown in Table 1. All of these tests were conducted with a single sliding pass. The length of that sliding pass is 120 mm.

The 4340 slider had a blanchard ground surface finish which was characterized by using a surface profilometer and standard ANSI definitions. The measurements were made perpendicular to the lay with a 2.5 mm profile sampling length. Over 200 separate profile measurements were made and are reported as combined averages. The measured surface roughness was R_q = 1.4 μm (root mean square deviation of the roughness profile), R_a = 1 μm (arithmetic average of the absolute values of the measured profile height), and an average maximum peak height of R_p = 3.0 μm. The average maximum peak height was determined using a 0.8 mm evaluation length averaged over a 2.4 mm sampling length.

To further characterize the surface asperities of the hardened slider, peak counts for various peak heights were measured, as well as the bearing area curve. These three measurements were used to estimate the average spacing of the asperities and their wedge angle near the tip. The average number of peaks, which are greater than 0.5 μm above the zero line, is 7.7/mm, while the average number of peaks, which are greater than 1.25 μm above the zero line, is 2.0/mm. The wedge angle of the asperities was estimated as between 5 and 10°.

Table 1 Friction test conditions

Normal pressure, MPa	Sliding speed, mm/s	Sliding distance, mm
12.0	25	120
21.5	25	120
16.7	0.25	120
22.7	0.25	120

After friction testing, one of each pair of sample test blocks was electroplated using a Woods nickel strike followed by copper to protect the surface during metallography. The plated samples were cross-sectioned parallel to the sliding direction so that samples could be viewed in the plane which contained the largest shear strains. One side of each of the cross-sectioned samples was polished for viewing in the scanning electron microscope (SEM). The other side was sliced into 2.5 mm thick cross-sections for transmission electron microscopy (TEM) samples.

The thin foils were prepared from these cross-sections by first grinding both sides with 600 grit paper to a thickness of 120 μm, then dimpling with cubic boron nitride to a thickness of 20-25 μm. Great care was taken to avoid introducing any damage to the soft copper during sample preparation; each step removed the damage of the previous step. This technique was verified on samples of annealed copper.

The electron transparent hole was made using a low angle (2° to 4°) ion milling process (Ref 27). A low ion beam angle was used to minimize ion mill damage in the copper. The two electron optic techniques were complementary to each other and provided a wide range of magnifications from 25× to 400,000× from which to view the subsurface deformation. Scanning electron microscopy was used to reveal the depth and localized heterogeneity of subsurface deformation along the entire 25.4 mm sample length, while TEM was used to study the fine details of the subsurface structures at higher magnifications.

3. Results

The variation in friction coefficient and the von Mises equivalent stress (i.e., computed from the combined shear and normal stresses) versus sliding distance for the four friction tests is shown in Fig. 3(a) and (b). The von Mises stress is given by:

$$\sigma_{vM} = \sqrt{\sigma_n^2 + 3\tau_i^2} \quad \text{(Eq 1)}$$

where the interfacial shear stress and the normal stress are defined respectively as (Fig. 1):

$$\tau_i = F_s/2A_{surf}$$
$$\sigma_n = F_n/A_{surf}$$

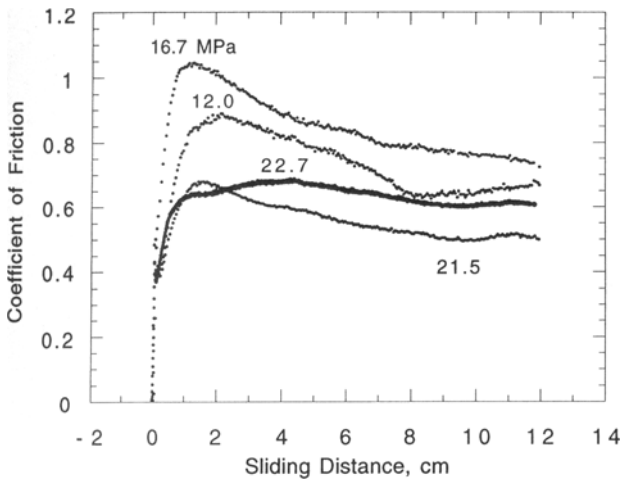

(a)

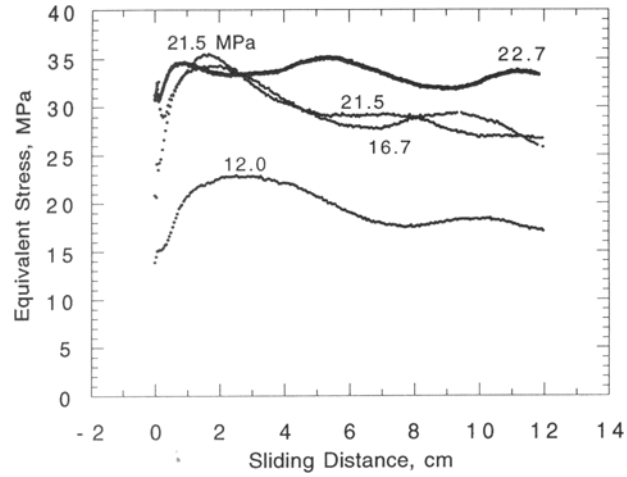

(b)

Fig. 3 (a) Coefficient of friction and (b) sample scale von Mises equivalent stress vs. sliding distance during sliding of copper. The normal pressure is shown for each curve. The respective sliding speeds are found in Table 1.

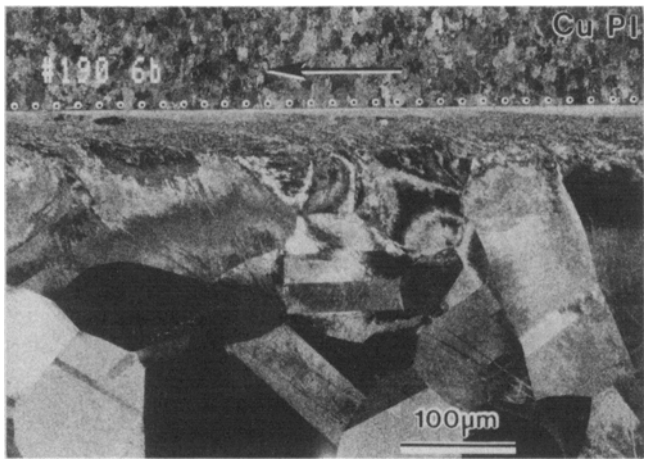

(a)

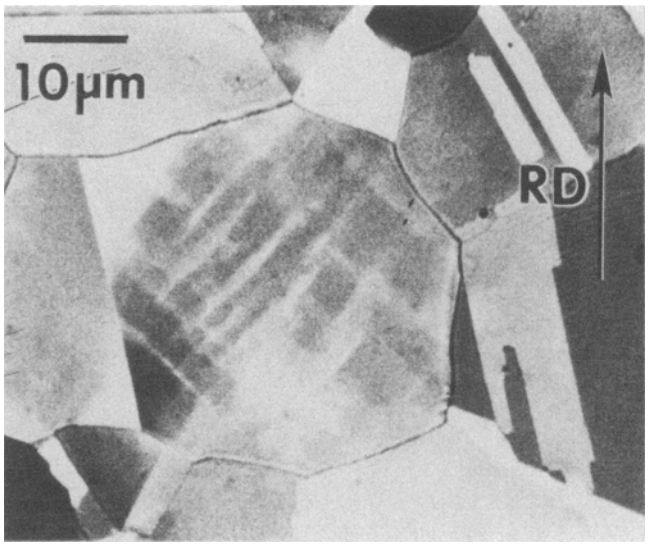

(b)

Fig. 4 (a) Localized shear deformation is observed in the subsurface layers of a cross-sectioned friction sample following sliding with a normal pressure of 17 MPa and at a sliding speed of 0.25 mm/s. The depth of this shear deformation ranges from 150 to 250 μm in this backscattered electron image. Contrast fringes within a grain are the result of the orientation changes which occur at the dislocation boundaries created during sliding. The grains at the the bottom of the micrograph have an even contrast and are thus nearly undeformed, whereas the contrast fringes have an increasingly finer spacing the nearer the region is to the surface. Within 5 to 10 μm of the surface the deformation structure is so fine that it appears as a bright band of contrast. The sliding direction is marked with an arrow. The boundary between the surface of the friction sample and the copper plating (Cu Pl) above it is indicated by a dotted line. (b) The backscattered electron image is very sensitive to low degrees of deformation as shown by this image of dislocation boundaries in Cu deformed 5% by rolling. The rolling direction is marked RD in this longitudinal plane cross section.

where F_s is the shear force (parallel to the surface); F_n is the normal force, and A_{surf} is the nominal area of contact. The friction coefficient increased initially with sliding distance to a peak value and then decreased. Note that the value of the coefficient of friction just as sliding began, 0.4, was similar for all tests. Subsequently, however, the friction coefficient depended on both sliding speed and normal force/pressure.

Comparison of the surface roughness of the steel platen before and after testing showed a slight but statistically significant change in roughness. The value of R_p decreased by 0.25 μm and R_a decreased by 0.03 μm indicating some slight wear of the surface during a test. Flakes of copper could also be observed on the steel platen. In contrast the surface roughness of the copper sample blocks increased significantly during testing from an R_a of 0.3 to an R_a of 0.5 μm.

The subsurface microstructures which developed during these tests are shown in Fig. 4-15. Note that all of the SEM and TEM micrographs are from the cross-sectioned friction samples and viewed along the longitudinal side parallel to the slid-

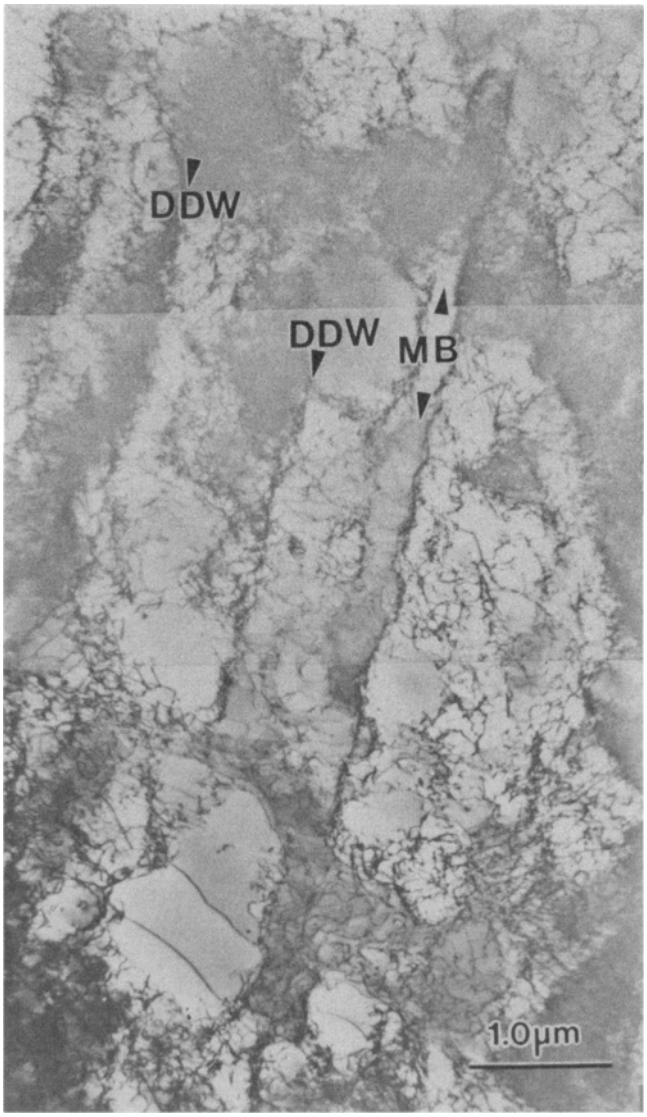

Fig. 5 The deformation structure 100 μm below the surface is composed of parallel dense dislocation walls (DDW) and microbands (MB) surrounding cell blocks. TEM micrograph of a cross-sectioned friction sample following sliding with a normal pressure of 17 MPa and at a sliding speed of 0.25 mm/s.

ing direction. Typical for all of these tests was the nonuniform deformation that occurs during sliding in the near surface regions, and results in a gradient of deformation microstructures. An example of this gradient in the near surface microstructures is shown in the SEM micrograph of Fig. 4(a). Figures 4(a) and (b) are backscattered electron (BSE) micrographs, which reveal changes in crystal orientation by changes in contrast density. Changes in orientation, and thus contrast, occur across grain boundaries, twin boundaries, and across dislocation boundaries. Dislocation boundaries are created during deformation and their occurrence thus delineates the regions of surface deformation.

This method is quite sensitive to deformation as shown by the structure in Fig. 4(b). Figure 4(b) is from a copper sample lightly cold rolled to a 5% reduction, which is introduced as a means of comparison with the friction-induced microstructures. The intersecting bands of white contrast correspond to paired dislocation boundaries within the central grain. Thus, the back scattered contrast can reveal where deformation has occurred, even if that deformation is not yet large enough to cause any resolvable distortion of the surrounding grain or twin boundaries.

It should also be noted that the degree of contrast change is not related to the degree of orientation change. For example, small changes in orientation may make large changes in contrast. Also, if the dislocation boundaries are spaced closer than the resolution limits in the SEM, several dislocation boundaries may be represented by one line of contrast change. Regardless of these caveats, however, an increasing fineness in the spacing of contrast changes does indicate an increasing refinement in the deformation microstructure and an increase in the degree of deformation.

With those guidelines one can interpret the contrast changes below the sliding surface in Fig. 4(a). The grains at the bottom left of Fig. 4(a), which are about 300 μm below the sliding surface, have a very even contrast across them and are thus undeformed. The grains and regions of grains at about 200 μm below the surface are beginning to show broad fringes of contrast changes within them, indicating that they contain a deformed microstructure. Within many of the broader contrast fringes are weaker contrast changes in a checkerboard like pattern. This pattern indicates evidence of a finer underlying structure.

Both the wider fringes of contrast and the contrast changes within the fringes are closer together and more abrupt the nearer the region of view is to the sliding surface. This indicates that the dislocation boundaries are spaced on a finer scale the closer the region is to the surface. Within about 10 μm of the surface the structures are so fine that they are not resolved in the SEM and thus appear as a light strip. Occasionally, a few larger structures are apparent just below this fine near surface structure. These larger regions are new recrystallized grains.

Note that there are local variations in the degree of deformation and depth of deformation along the sliding interface. Although there are variations in the microstructure over small distances of about 150-300 μm, the average appearance of the microstructure was similar over the entire 25.4 mm length for most of these centerline cross-sectioned test blocks. The effect of the sample corners on deformation appeared to extend only about 200 μm along the sliding direction at both corners. Unfortunately, some unevenness in loading was observed in one sample and that uneveness was reflected in the depth of subsurface microstructures (Ref 26).

The types of deformation structures which cause the contrast change in the SEM micrographs of Fig. 4 are shown in greater detail using TEM. Note that the nomenclature used for the observed dislocation structures follows the definitions provided in Ref 28 and 29. Figure 5 shows an example of the dislocation structures which have developed during sliding at a region that is about 100 μm below the sliding surface. This region contains parallel sets of long dense dislocation walls (DDWs) and microbands (MBs) with dislocation cells in between the DDWs.

Fig. 6 The deformation structure 20 μm below the surface is composed of lamellar boundaries (LB) nearly parallel to the sliding direction. Dislocation cells are found in between the lamellar boundaries. A few equiaxed subgrains (ES) are also observed. The sliding direction is marked with an arrow in this TEM micrograph of a cross-sectioned friction sample following sliding with a normal pressure of 12 MPa and at a sliding speed of 25 mm/s.

Fig. 7 The deformation structure from 0.5 to 6 μm below the surface is shown in this TEM micrograph of a cross-sectioned friction sample following sliding with a normal pressure of 12 MPa and at a sliding speed of 25 mm/s. The structure is composed of lamellar boundaries (LBs) nearly parallel to the sliding direction, cells, and equiaxed subgrains (ES). The microstructures at the top of the figure continue to the surface but at a slightly reduced size scale. The extremely fine long lamellas nearest the surface at the top of the figure contain both cells and deformation twins, whereas the LBs shown in the bottom of the figure contain only cells. Note the many equiaxed subgrains found at the bottom of the figure. The sliding direction is marked with an arrow. The location of the surface is indicated with a line in the top righthand corner and was extrapolated from an adjacent region in the TEM thin foil. The wavy diagonal line at the top righthand side of the photo is just the edge of the TEM thin foil.

The 2 μm spacing of DDWs in this area suggests that this region has been deformed to a von Mises equivalent strain of 10-20% ε_{vM}. At a distance of 20 μm below the sliding interface, the dislocation structure contains many closely spaced lamellar dislocation boundaries (LBs), which are nearly parallel to the sliding surface and equiaxed subgrains (Fig. 6). These boundaries are spaced 0.23 μm apart. Dislocation cells are found in between the lamellar boundaries.

Examples of the surface structures from 0 to 5 μm below the surface are shown in Fig. 7 and 8. The long lamellar boundaries are similar to those in Fig. 6 except that their spacing is much finer the closer the region is to the surface. This extremely fine region nearest the surface, e.g., Fig. 8 and top half of Fig. 7, stands out from the adjacent region below (bottom half of Fig. 7), even though the region below has a relatively small microstructural spacing of about 200 nm. While the demarcation between these regions is clear, it is not a sharp single boundary; rather it is a string of lamellas which have various widths and lengths and makes a smooth structural transition between the two microstructures.

The demarcation between the structures in two surface regions is shown in plots of the spacing of lamellar boundaries

Fig. 8 Very fine lamellar boundaries immediately below the surface. The surface is marked by a dotted line.

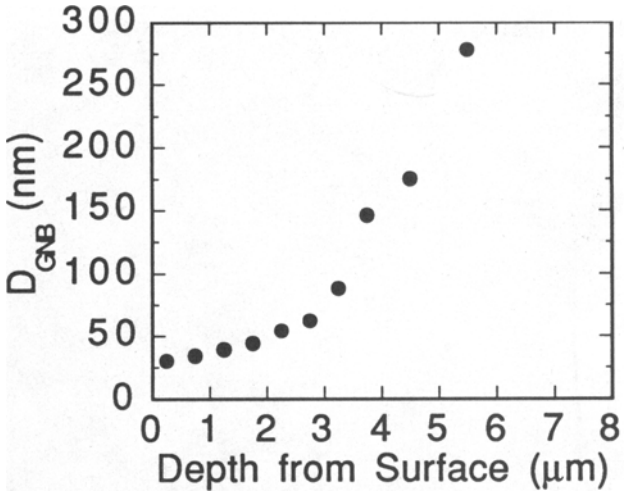

Fig. 9 The spacing of dislocation boundaries, D_{GNB}, is plotted versus depth from the surface. Note the change in the slope of this curve at a 3 μm depth. Below 3 μm the size scale changes slowly, whereas above that value the size scale increases rapidly with depth. Overall there is an order of magnitude change in the size scale of the microstructure in a distance of 6 μm. The spacing was measured as the average of linear intercepts taken along the direction of the minimum spacing between the long lamellar boundaries. This average spacing includes both lamellar boundaries and equiaxed subgrains. Data are from a cross-sectioned friction sample following sliding with a normal pressure of 12 MPa and at a sliding speed of 25 mm/s.

versus depth from the surface in Fig. 9. Each data point in Fig. 9 is the average of from 40 to 100 measurements taken at several locations along the sliding direction at that particular depth. The spacing of these lamellar boundaries increases steadily as one moves away from the surface, from the smallest spacing of 35 nm at a depth of 0.5 μm below the surface to about 200 nm at a depth of 5 μm.

Figure 9 also shows that there is a smooth but definite change in the slope of the spacing versus distance from the surface occurring at a depth of 3–4 μm for this sample. In general the depth of this rapid increase in boundary spacing varied sporadically along the sliding length and also increased on average with increasing normal load. Thus, the observed depths containing the fine region varied from 1.5 to 15 μm below the surface. These variations are observed in the SEM micrographs like Fig. 4, in which the top strip of unresolvable bright contrast is equivalent to the extremely fine near surface lamellar boundaries observed in the TEM.

Three other features distinguish the two subsurface layers. First the deeper region, represented in the lower half of Fig. 7, is composed of many more equiaxed subgrains mixed with the lamellar boundaries than were observed either in the top of Fig. 7 or in Fig. 8. There are also more equiaxed subgrains than observed deeper in the structure (Fig. 6). Note that a few of the large equiaxed subgrains in Fig. 7 (marked ES) are three times the size of the surrounding structure.

Second, deformation twins are observed within the very finely spaced lamellar boundaries in the top half of Fig. 7 and in Fig. 8 but not in the wider lamellas. These twins and the lamellar boundaries are shown at higher magnification in Fig. 10(a) and (b). The twins were found in the very finely spaced lamellar boundaries from 0-3 μm below the surface in this example.

Third, there are slight differences in chemical composition. The fine structures observed in Fig. 7-10 are primarily copper but they also contain slight amounts of iron (from the steel platten) within 2 μm of the surface as found by energy dispersive "x-ray" spectrometry (EDS) measurement. No iron was found below 2 μm in that sample. Preliminary EDS measurements did not show any evidence of oxygen but those measurements should be made again to see if trace quantities of oxygen can be resolved. Very little diffraction change or evidence was found for mixed-in oxides or other elements, such as iron, from the counterface so that the Fe in the copper layers found by EDS must be finely distributed.

In contrast to Fig. 7, some regions had a recrystallized structure just below the very fine near surface lamellar boundaries. This recrystallized region is shown in the TEM micrograph of Fig. 11 and in the backscattered SEM images of Fig. 12. The new recrystallized grains appear in the SEM micrographs as large islands of even contrast in the midst of the much finer structures. In the TEM micrograph (Fig. 11) the recrystallized regions are nearly dislocation free and curve into the deformed regions with high angle boundaries.

Figure 12(a) also illustrates how some regions have recrystallized (far left and far right edges just below the surface of Fig. 12(a)) while adjacent regions along the sliding direction have not recrystallized (center just below the surface of Fig. 12(a)). If one were to view the left and right regions of Fig. 12(a) in the TEM it would look similar to Fig. 7, whereas the center of Fig. 12(a) would look similar to Fig. 11 in the TEM.

The recrystallized regions were more frequently observed in tests which were at the higher sliding rate and having higher

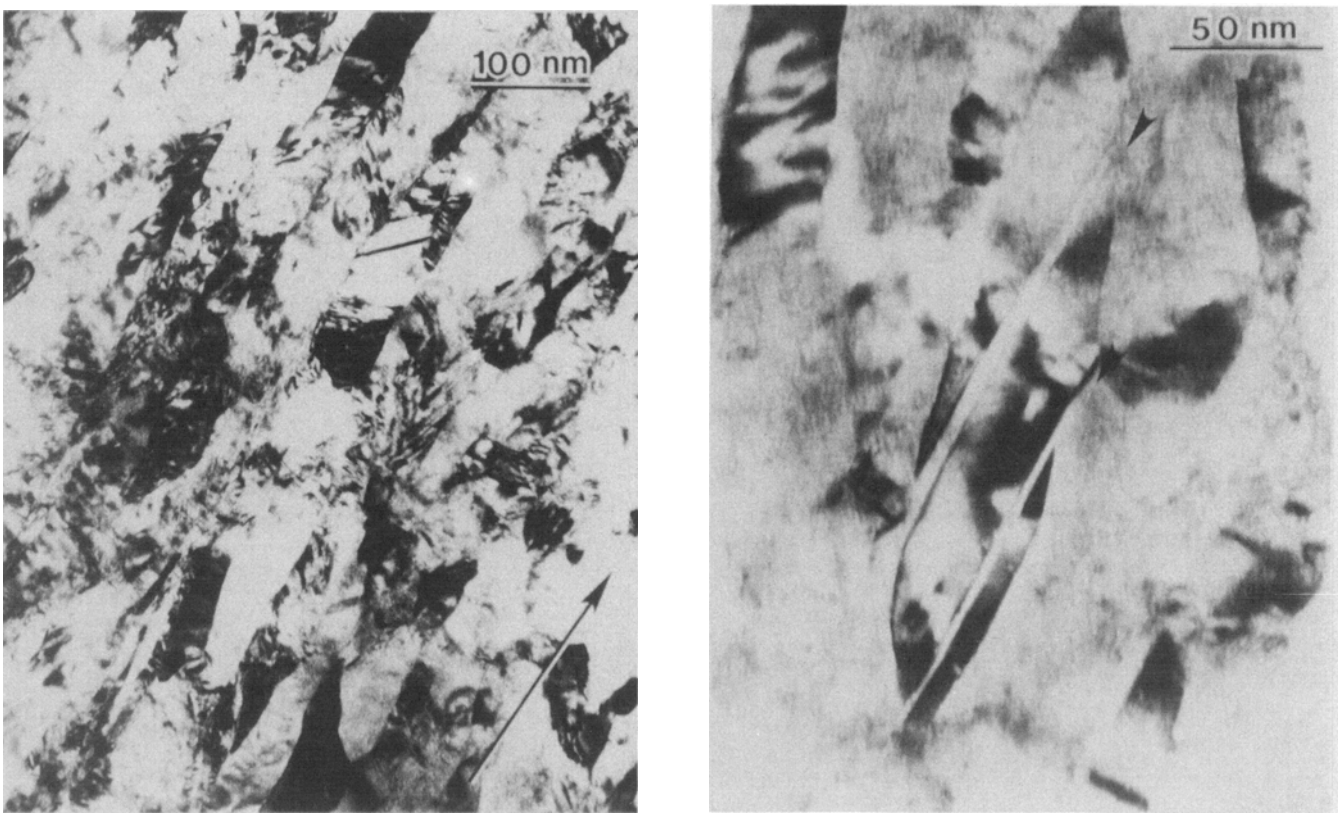

(a) (b)

Fig. 10 (a) A high magnification view of the very fine scale structure found just below the surface of a cross-sectioned friction sample following sliding with a normal pressure of 12 MPa and at a sliding speed of 25 mm/s. Lamellar boundaries, cells and deformation twins are formed. The sliding direction is marked with an arrow. (b) Narrow deformation twins within a lamella are marked with arrows.

normal loads. For example, compare Fig. 12(a) for a test at the low sliding rate of 0.25 mm/s with widely spaced recrystallized regions, to Fig. 12(b) with nearly a continuous region of recrystallized grains following sliding at the higher rate of 25.4 mm/s. The widely spaced recrystallized regions can range from 3 to 20 μm in depth by 5 to 200 μm in length spaced about every 100 μm for the case of the slow sliding rate. Typically, like Fig. 12, these recrystallized regions are sandwiched in between the extremely fine lamellar boundaries near the surface and the less deformed region with a coarser dislocation structure.

However, sometimes the recrystallized region has either originated in the fine lamellar boundaries at the surface or else grows into and consumes those very fine lamellar boundaries. In other cases the BSE images showed regions with alternating layers of very fine deformation structures and coarser recovered subgrains/recrystallization nuclei. Frequently there is some contrast evidence indicating that the regions which recrystallized have been deformed again by additional sliding after recrystallization.

The backscattered electron micrographs provide a measure of the frequency and distribution of the various types of microstructures along the sliding length. This includes not only the amount and location of the recrystallized region but also the region of very fine lamellar structures, the gradient in the coarser and thus less deformed structures, changes in surface topography, and any mixing and folding over of the surface layers.

Table 2 The effect of normal pressure on the average subsurface depth of the region with an extremely fine spacing of lamellar boundaries

Normal pressure, MPa	Sliding speed, mm/s	Average subsurface depth of nanometer spaced lamellar boundaries, μm
12.0	25	4.4
21.5	25	7.3
16.7	0.25	6.8
22.7	0.25	7.5

For example, some periodicity in the depth of the very fine lamellar boundaries along the sliding length was observed. This depth varies from a minimum of 1.5-3 μm to a maximum of 5-15 μm over a wavelength of about 150 to 200 μm of sliding length. The average values for this depth as a function of normal pressure are shown in Table 2. The average depth increases with increasing load.

The strain gradient in the less deformed structure and the depth of deformation also varied locally along the sliding length by roughly a factor of two. The "less" deformed structure is still highly deformed and has a very large strain gradient. An example of the strain profile obtained from the displace-

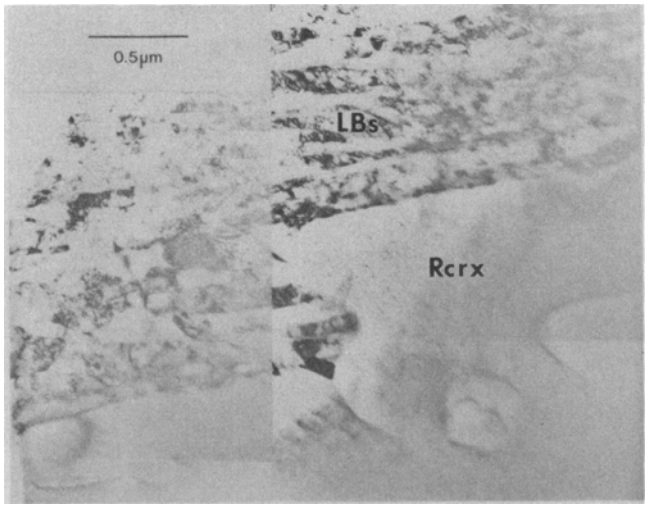

Fig. 11 Recrystallized region (Rcrx) nucleated below the region of very fine lamellar boundaries (LBs) in a cross-sectioned friction sample following sliding with a normal pressure of 22.7 MPa and at a sliding speed of 0.25 mm/s. (Note that the fine spots in the recrystallized region are dislocation loops caused by ion beam damage during sample preparation.)

ment of twin boundaries which were perpendicular to the sliding direction is shown in Fig. 13.

The surface roughness observed in the SEM cross sections was generally consistent with the very fine surface roughness measured with the profilometer after testing. However, every several hundred μm, a section of the near surface layer appeared to have been removed as shown in Fig. 14. These features were uncommon on the half of the sample towards the entrance side of the slider and somewhat more common on the exit side. This removed layer could be shallow and short, e.g., 2 μm deep and 5 μm long as in Fig. 14(a), or relatively deep and long, e.g., 10 μm deep and 100 μm long like Fig. 14(c). Frequently, the material exposed at the new surface had been recrystallized.

More commonly observed than this rough surface was the observation of folds embedded in the very fine surface layers as in Fig. 14(a) and 15(a-c). These folded layers are pressed into the surface and incorporate oxides and voids at the folds. One can imagine that these folds could originate both from the rolling over and pressing in of the large asperities created from shaving off the surface layers like Fig. 14(b and c) as well as from the deposition of the flakes which have been shaved off.

Copper flakes were also deposited on the steel platen during sliding. The black regions surrounding these folds in the copper sample are both particles and voids as determined by comparing the secondary electron image with the back scattered image Fig. 15(b and c) and by using EDS. The large pressed-in particles containing iron in Fig. 14(a) and 15 are from the steel counterface. The folding and pressing in of materials from other regions and the removal of surface layers change the microstructure of the near surface layers. This layering of different structures is very apparent in Fig. 15, in which recovered subgrains and recrystallized regions have been pulled up and

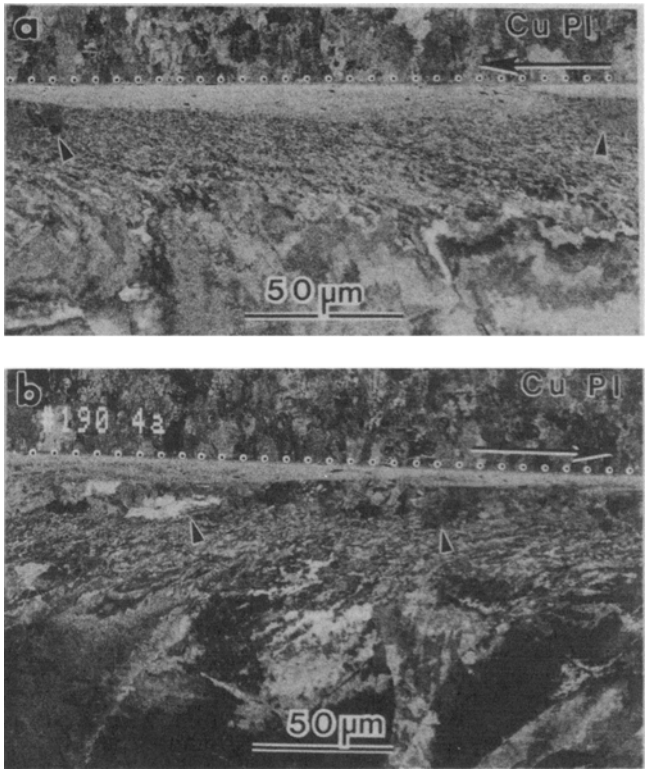

Fig. 12 Dynamically recrystallized regions (marked by short arrows) are found below the very fine lamellar boundaries in this BSE image. The LBs make a bright band of contrast at the surface. The amount of recrystallization occurring during a test increased with increasing normal pressure and sliding speed. The sliding direction is marked with an arrow. The boundary between the surface of the friction sample and the copper plating (Cu Pl) above is indicated by a dotted line. (a) A cross-sectioned friction sample following sliding with a normal pressure of 17 MPa and at a sliding speed of 0.25 mm/s. The recrystallized regions are not continuous but are in isolated regions along the sliding length. (b) A cross-sectioned friction sample following sliding with a normal pressure of 21 MPa and at a sliding speed of 25 mm/s. The recrystallized regions are nearly continuous across the sliding length.

smeared over the folded-in particles from the counterface and fine lamellar structures.

4. Discussion

The observed subsurface microstructures included dislocation structures formed by subsurface deformation, deformation twins, newly recrystallized grains, highly recovered large subgrains, and mechanically mixed copper and iron. These structures were observed at different depths from the surface. Similar features have been observed during wear experiments conducted at smaller loads and for longer sliding distances (Ref 3-6). These different microstructures typically arise from differing stress, strain, strain rate and thermal conditions and provide strong clues on the local deformation history in the subsurface regions. By combining the microstructural evi-

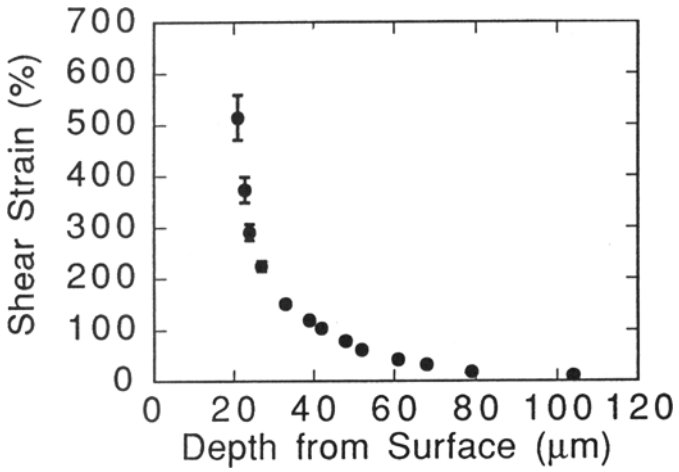

Fig. 13 Strain profile with depth below the surface as measured by the sheared boundaries of annealing twins oriented perpendicular to the surface. Taken from the cross-sectioned friction sample following sliding with a normal pressure of 17 MPa and at a sliding speed of 0.25 mm/s.

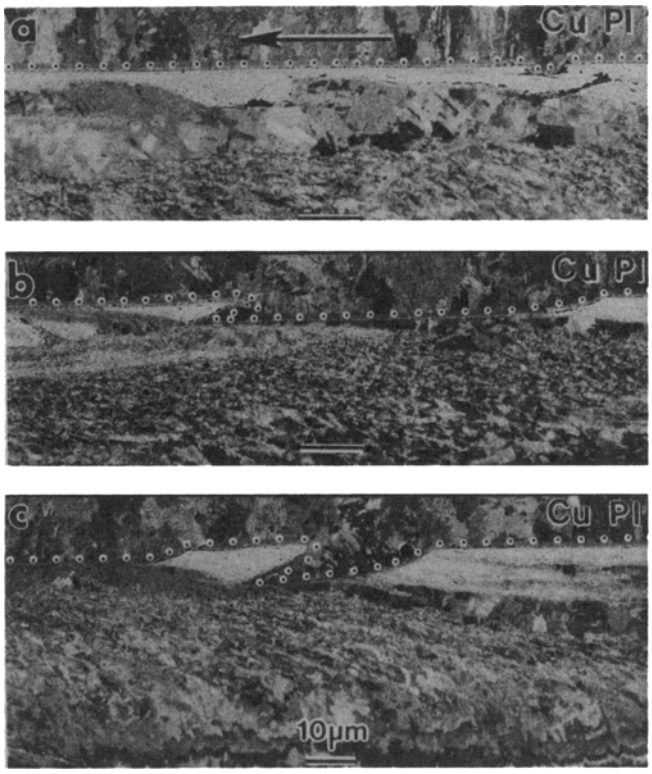

Fig. 14 Large surface asperities and valleys are created where the sliding action has shaved off thin surface layers. This roughness is indicated by the dotted lines marking the boundary between the surface of the friction sample and the copper plating (Cu Pl). BSE images of a cross-sectioned friction sample following sliding with a normal pressure of 17 MPa and at a sliding speed of 0.25 mm/s. The sliding direction is marked with an arrow at the top of (a) and is in the same direction for (b) and (c). The straight markers indicate the length of 10 μm in the figures. (a) Small, 10 μm long by 2 μm deep, flake-like region removed from the very fine lamellar structure at the top. These flake-like surface layers are deposited and pressed into nearby surface layers. For example, the black iron containing particles at the interface between the very fine structure in a band of white contrast and the recrystallized region indicate that part of this top surface layer was either formed through the deposition or extrusion of a shaved off flake from a nearby region. (b) A 60 μm long by 3 μm deep region removed leaving a small tongue of material. Note that the recrystallized layer is exposed by shaving a thin section of the top layer. (c) Another deep and long valley (9 μm by 25 μm) and a large asperity. A second removed layer begins at the left of the micrograph and extends beyond the edge of the photo for 200 μm.

dence, the bulk stress-strain properties of copper and the mechanics of the sliding process, it is possible to make some semi-quantitative estimates and bounds on the deformation.

4.1 *Comparison with Wear Studies and Bulk Deformation*

Microstructural observations following wear experiments have typically found three to four zones of subsurface microstructures (Ref 5, 6). Zone 4 is the compositionally/mechanically mixed region within the very top surface layers. Zone 3 is a highly deformed region which may have recrystallized during sliding. Zone 2 is a plastically deformed subsurface region. Zone 1 is simply the remaining bulk microstructure which is generally undeformed, but, may be slightly deformed if the nominal loads are above yield. While these zones are typical, all four may not be present at the same time for a given set of test conditions and the boundaries between them may blur. For example if recrystallization or extended recovery does not occur there is no demarcation between Zones 2 and 3 in this definition.

4.1.1 Zone 4

A definite near surface layer was developed in our tests which can be compared to the compositionally/mechanically mixed Zone 4. This layer began at the surface and was from 1.5-15 μm deep, depending on the test conditions and also the location within the sample. The local depth of Zone 4 could be decreased either by recrystallization or the removal of surface layers by the sliding action. Alternatively the depth could be increased by the deposition of a copper wear flake.

Our Zone 4 is not fully developed compared to the typical Zone 4, but it does share some important characteristics. Our Zone 4 is demarcated by an extremely fine size scale, 30-50 nm, of dislocation boundaries which are of the same fine size scale as other mechanically mixed regions (Ref 4, 6, 8). Thus, this region stands out from the rest of the microstructure even though Zones 2 and 3 also have relatively small microstructural size scales.

In other work the boundary between zones 4 and 3 typically makes a very sharp line (Ref 3, 6), whereas in ours the boundary is clear but not sharp. While a mechanically mixed region develops relatively quickly in wear experiments, this layer requires a certain sliding distance (i.e. >0.3 m in Ref 6) and many wear cycles to develop fully. For our tests the sliding length of 120 mm is three orders of magnitude smaller than the typical

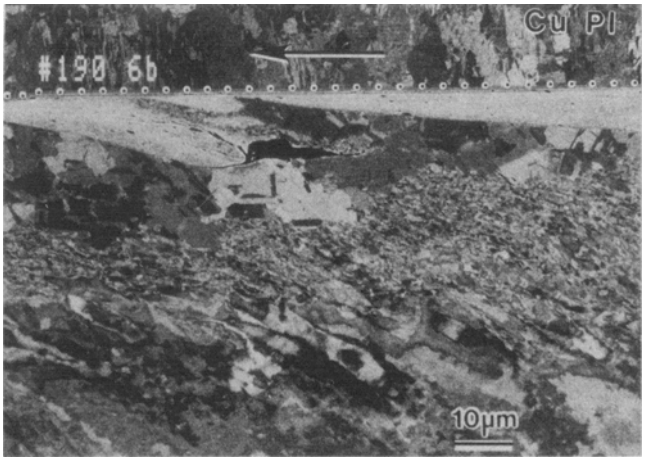

(a)

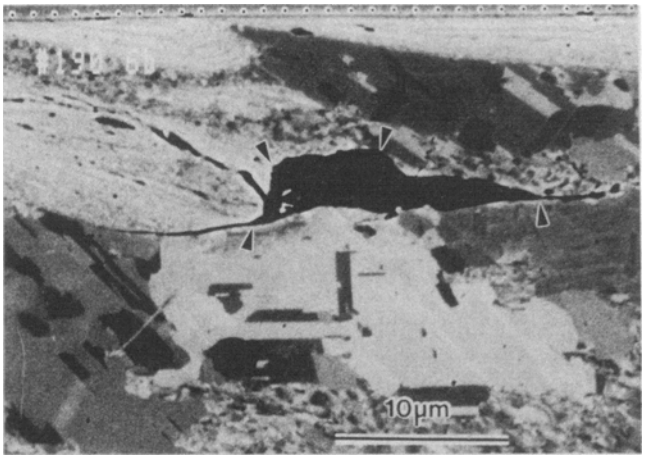

(b)

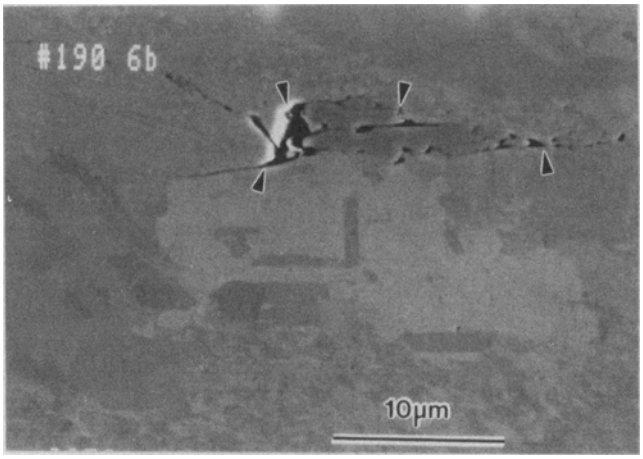

(c)

Fig. 15 A series of higher magnification views of the mixing of surface layers in a cross-sectioned friction sample following sliding with a normal pressure of 17 MPa and at a sliding speed of 0.25 mm/s. (a) A tongue shaped piece of the fine lamellar region which appears in bright contrast at the top left has been pressed farther into the subsurface by the extrusion or dragging of adjacent material up and over this tongue by the sliding action. (b) Enlarged BSE image at the fold. Note that the curved interfaces between the recrystallized regions and the fine structure in the deformed areas is also especially apparent in this photo. (c) Secondary electron image of the black region surrounded by arrows in (b) showing that this region contains small voids and particles. The particles contain iron from the counterface and are possibly iron copper oxides.

wear experiment which may have sliding distances as large as 500 m.

On the other hand, our larger loads aid in forming Zone 4. Thus, one expects the beginnings of a compositionally/mechanically mixed region but not a fully developed one. This expectation is borne out by the results in which some surface layers are folded under incorporating iron-containing particles below the surface, the pressing in of copper wear flakes, and by the fine dispersion of iron within the extremely fine lamellar region found by EDS in the TEM. This is also consistent with the very slight decrease in peak heights and surface roughness observed for the steel platen following a test.

In wear studies the impression is given that the extremely fine size scale of the microstructure in Zone 4 is largely a result of the mechanical mixing of extremely fine wear particles, which are embedded and dispersed throughout the very near surface layers. This mechanism is certainly very important for the case of very large sliding distances. Mechanical mixing is not, however, the main source of microstructural refinement in our Zone 4. First the long lamellar boundaries share the important characteristics of lamellar boundaries, which form at large strains during either rolling or torsion deformation within Stage IV (Stage IV is a deformation regime of nearly constant strain hardening observed at large strains.) (Ref 29-33). Albeit the lamellar boundaries in the current study are on a much finer size scale than found during conventional bulk deformation (Ref 29-33). There is also a smooth gradient in size scale of these boundaries with respect to the depth below the surface. Further, many large areas of the very fine lamellar boundaries contained only the virgin copper and no other elements. Thus,

the fine size scale observed in zone 4 in this case is primarily the result of tremendous shear strains occurring very near the surface. This idea will be developed further in the next sections.

Although deformation-induced temperature effects have not been considered for Zone 4, this layer will also become warm at the same time as the layer below it due to deformation-induced temperature increases. However, this top layer loses heat to the platen and thus may not be as warm as the layer underneath it. Further, temperature effects on the microstructure such as subgrain growth and recrystallization may be inhibited by the fine dispersion of Fe and possibly oxide in this region.

4.1.2 Zone 3

In this zone the deformation microstructure has been clearly affected by deformation-induced temperature increases, resulting in dynamic recrystallization and/or subgrain growth. Both of these effects have been observed in these tests in which a discontinuous recrystallized layer was observed in the BSE images as well as in the TEM. This layer generally began below Zone 4, at a depth 3 to 10 μm and extended as deep as 20 μm. Occasionally, however, a recrystallized region consumed the regions right up to the surface.

The location of the recrystallization nuclei suggests that the narrow transition region between Zone 3 and 4 provides good sites for recrystallization nuclei, possibly due to higher misorientations in this region. Subgrain growth and the development of dislocation structures at higher temperatures are more ambiguous to define than recrystallization. However, the size scale of the microstructure as well as the shape anisotropy of the microstructure provide strong clues.

There is a clear tendency for equiaxed structures to develop in greater proportion with increasing temperature (Ref 34, 35). A larger proportion of equiaxed subgrains was observed in this region, many with a diameter of three times that of the surrounding structure. Those features strongly suggest the occurrence of subgrain growth and the effect of increasing temperatures above ambient temperature. High purity, highly deformed copper is known to dynamically recrystallize at fairly low homologous temperatures (Ref 30). Thus, the temperature increase in these subsurface zones need have been only 100-200 K.

4.1.3 Zone 2

In this zone, localized deformation has created dislocation structures which are relatively unaffected by the much smaller deformation-induced temperature increases. For our studies, this zone begins below Zones 4 and 3 roughly at 5-20 μm below the surface and extends to 100 to 300 μm in depth. This range of Zone 2 is consistent with other wear studies (Ref 3, 4, 6). Generally the microstructure in this region has simply been described as containing equiaxed cells. However, it has been found that other dislocation boundaries, such as DDWs, MBs, and LBs, are created during bulk deformation in addition to dislocation cells (Ref 28, 29, 32-40). These additional dislocation boundaries have been observed in the present friction samples and will be used in the next sections to infer the stress and strain state within this zone.

4.2 *Inferring the Local Deformation History from the Microstructure*

4.2.1 Framework for the Evolution of Deformation Microstructures

A general framework for the evolution of deformation microstructures for medium to high stacking fault energy fcc metals has been developed (Ref 28, 29, 33, 36-40). This framework, called grain subdivision, is based on the following principles: (1) there are differences in the number and selection of simultaneously acting slip systems among neighboring volume elements, and (2) the dislocations formed during plastic deformation are trapped into low energy structures (LEDS). This framework enables one to quantitatively describe the consistent and gradual changes in the microstructure which occur with increasing stress and strain. This framework also enables one to better interpret the dislocation microstructures occurring at a sliding interface and thereby infer the stress and strain state.

The general framework of grain subdivision includes the formation of rotated volume elements at two sizes for all deformation modes. At the larger size scale, the rotated volume element is called a cell block and, as the name suggests, contains from one to several dislocation cells. Each cell block slips on a different number and selection of simultaneously acting slip systems than its neighboring volume elements. While theoretically five slip systems are required to make any arbitrary shape change for homogeneous deformation as set forth by Taylor (Ref 41), fewer slip systems than required by Taylor are favored within each cell block to minimize the energy increase associated with large numbers of intersecting slip systems (Ref 28, 29, 33, 36-39). Intersecting slip systems, for example, increase the flow stress and energy through dislocation jog formation. Although the number of slip systems operating within an individual cell block is less than that required for homogeneous (Taylor) deformation, groups of cell blocks collectively act to approximate the Taylor criterion.

The cell blocks are bounded by long dislocation boundaries that accommodate the lattice misorientations, which result from glide on different slip system combinations in neighboring cell blocks. The boundaries which accommodate these lattice misorientations are called geometrically necessary boundaries (Ref 42) and include DDWs, MBs, and LBs. The dislocations in these boundaries are also arranged to mutually screen their individual stress fields. Cell blocks are further subdivided by ordinary cell boundaries which have been termed incidental dislocation boundaries. These incidental boundaries form as a result of statistical trapping of glide dislocations supplemented by forest dislocations (Ref 42). In previous studies these two types of boundaries have been quantitatively characterized by their macroscopic orientation to the deformation axis, crystallographic orientations, frequency of occurrence, and the morphology of the boundary.

From this quantification it has been observed that the DDWs, MBs, and LBs have special macroscopic orientations with respect to the macroscopic deformation axis. Thus, they provide some evidence for the type of stress state which created them. Furthermore, the spacing of these boundaries decreases with increasing stress and strain so that a relationship can be

made between the flow stress of the material and the size scale of the microstructure.

4.2.2 Stress and Strain Concentrations in Zones 4, 3 and 2

Estimates of the strength and thus the local stress, strain, and strain rate in the deformed zones can be obtained from the microstructure. The very fine lamellar structure in Zone 4 contains many deformation twins. Single crystal studies have shown that the formation of deformation twins in copper requires a minimum critical resolved shear stress of 150 MPa (Ref 43). Deformation twins formed during shock loading of copper were also found to follow this criterion (Ref 44). A resolved shear stress of 150 MPa translates to an equivalent stress of 450 MPa based on an average Taylor factor of three. No preferred orientation is accounted for in this factor of three.

A value of 450 MPa provides a lower bound for both the flow stress of zone 4 and the size of the stress concentration that has developed in Zone 4. This stress concentration is at least a factor of 15 when the flow stress, which occurred locally, is compared to the applied maximum von Mises equivalent stress of 35 MPa based on the combined nominal shear and normal loads (Fig. 3(b)).

A local flow stress gradient versus subsurface depth can be estimated based on an extrapolation of the inverse relationship between the flow stress and the microstructural size (Ref 45). This extrapolation is justified based on the self similarity of the lamellar microstructure observed herein with that of lamellar microstructures developed during torsion and rolling deformation in Stage IV (Ref 30-32, 45). An extrapolation is needed as the microstructural size scale herein is three times smaller than that previously observed during bulk deformation.

For reference, the size scale of the microstructure generally changes by one to two orders of magnitude during deformation from large to small strains. The microstructural size scale is considered to be the largest contributor to the flow stress in this case. Two other lesser effects, which also contribute to the flow stress, are included in this estimate only to the extent that they change the microstructural size scale. These lesser contributors are: (1) the slight increase in iron and and possibly oxygen at the surface which will increase the flow stress by solute strengthening (and also decrease the microstructural size scale) and (2) any deformation-induced temperature increases which will decrease the flow stress and also increase the microstructural size scale.

The torsion data of Alberdi (Ref 31) shows that an increase in temperature of 100 K decreases the flow stress of copper at large strains by 15%, while a 200 K increase decreases the flow stress by 30%. However, a large part of this decrease in flow stress with temperature is directly reflected in the microstructural size scale. For example in nickel, which is an fcc metal like copper, an increase in temperature of 280 K decreases the large strain flow stress by 40% at the same time the microstructural size scale increases by 50% (Ref 32). With those caveats in mind, a flow stress estimate for the observed friction-induced deformation is made. A combination of data and equations from Ref 30-32 and the torsion data reported herein suggests the following relationship for the flow stress at large strains within Stage IV:

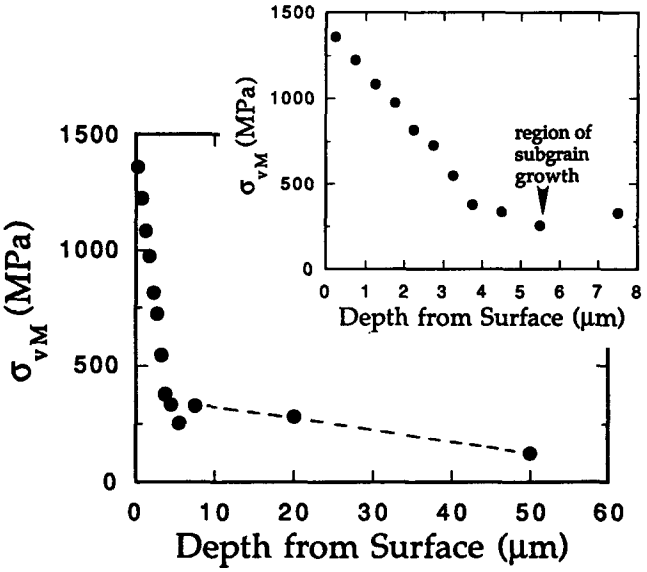

Fig. 16 Estimates of the equivalent flow stress of copper as a function of the depth below the surface based on the spacing of lamellar boundaries and equiaxed subgrains. Note the change in slope of this curve at a depth between 3 and 4 μm. This change in slope suggests that there are at least two overlapping stress fields contributing to the subsurface deformation.

$$\sigma_{vM} = 120\ \text{MPa} + 37.5\ \text{MPa}\ \mu\text{m}^{-1}/D_{GNB} \qquad \text{(Eq 2)}$$

To provide a frame of reference with other work, this equation may be equivalently written in terms of the crystallographically resolved shear stress via an average Taylor factor M of three:

$$\tau = \sigma_{vM}/M = \sigma_{vM}/3$$
$$\tau = \tau_0 + KGb/D_{GNB} \qquad \text{(Eq 3)}$$

Using the experimental values for copper of shear modulus G = 4.21×10^4 MPa and a Burgers vector b = 2.56×10^{-10} m, this formulation results in a constant factor K = 1.2 . This low value of K is consistent for Stage IV shear deformation (Ref 32).

This estimate of the flow stress versus subsurface depth is plotted in Fig. 16 using Eq. 2 and the microstructural data plotted in Fig. 9 and mentioned in the text. The stress at 50 μm in depth, however, was estimated from the stress-strain curve in Fig. 1 and a strain of 0.08 determined from a sheared twin boundary. This different method was required because Eq 2 does not apply for this small strain Stage III deformation regime. This estimate of the flow stresses with depth compares favorably to the location of deformation twins with depth in Zone 4 and the critical stress needed for their formation.

Note that the flow stress (and strain level) is largest at the surface and decreases rapidly with depth. There is also a change in the slope of the curve in Fig. 16 occurring at the transition between Zone 4 and 3. The flow stress decreases rapidly with depth in Zone 4. The decrease in flow stress in Zones 3 and 2 was much less rapid.

This estimate also shows that the work hardening potential and the size of the flow stress for copper are tremendously large when deformation is confined, as in these friction tests. Al-

though Fig. 9 is meant to be simply an estimate to illustrate the stress fields, there is no doubt that the extremely fine microstructural size scale of 35 nm at the surface must translate into very large stresses. These values, however, would be very difficult to obtain in bulk monotonic testing, as instabilities in sample geometry would introduce fracture and shear banding prior to reaching these values (Ref 46).

In an analogous manner, the highest strain level in Zone 4 is estimated by extrapolating the data in Ref 29-32 and comparing it to our microstructural size scale. Thus, the ε_{vM} at the surface is roughly 25. The maximum strain rates possible, assuming perfect adhesion during a straining event, are the sliding rates divided by the depth of deformation. These maximum shear strain rates are thus approximately 50/s for the slow sliding speed and 5000/s for the fast sliding speed using a Zone 4 depth of 5 μm.

Such maximum strain rates would only arise momentarily in the event that a local surface region adhered to the platen. In contrast, the time averaged estimates of the strain rates based on the estimates of total strain are much lower and provide a lower bound for the strain rates. The time averaged strain rates at the surface are about 0.05/s for the slow sliding speed and 5/s for fast sliding speed.

4.3 *Comparison with Friction Models*

Friction and wear models include those that consider local asperity interactions (a rough surface) and those that consider the effects of localized smooth body contacts (for example Hertzian) or a combination of the two (Ref 11-25). Both of these effects create local stress concentrations at the surface. However, the region of influence of their individual stress fields may differ.

For example, asperity interactions dominate a region very near the surface while Hertzian type stress fields extend deeper. While these models have been principally derived to calculate and explain the macroscopic friction coefficients and wear, these calculations also include in part the determination of the local stress and strain state, the depth and magnitude of the surface deformation and the location of the maximum stress and strain. Thus, one can compare these various models to the current observations of localized surface deformation and to our friction coefficient values.

Our microstructural observations suggest that there are two regions of surface deformation with different characteristic depths reflecting at least two different sources for the localized flow. The first region is the very near surface and highly deformed region of extremely fine lamellar boundaries (Zone 4). The second region extends an order of magnitude deeper and includes Zones 3 and 2. Also our observations show that the maximum stress and strain occur at the surface and not at some distance below the surface. All of these features will be considered in the model comparisons.

4.3.1 Idealization of the Current Test Geometry

An idealized representation of our test configuration is first presented in order to compare our results with various friction models and to illustrate the mechanics of contact and sliding. Our basic geometry is two nominally flat bodies in contact with an apparent area equal to the square surface area of the copper sample (Fig. 17(a)). While the contacting surfaces are nominally flat, they are not smooth. Rather these surfaces have a characteristic roughness which affects the interactions between the surfaces.

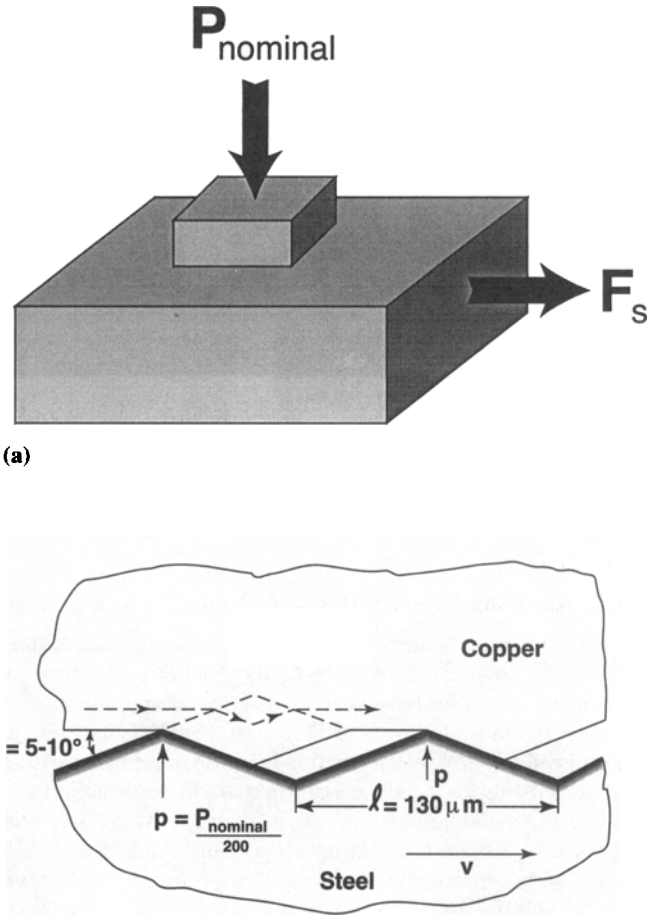

Fig. 17 Idealized configuration of the friction test set up for comparison with asperity deformation models. (a) Basic geometry. (b) During the test the indenting steel wedge causes a ridge of copper to develop (see text for details).

This roughness is idealized in the following way. First, because of the greater roughness, hardness and elastic behavior of the steel platen, only the surface roughness of the platen is considered. The surface of the copper is considered to be smooth initially for the purposes of analysis. The roughness of the steel platen is idealized as a series of wedges whose lay is perpendicular to the sliding direction (Fig. 17(b)).

The size and spacing of these wedges is obtained from the statistical roughness averages for the platen. Thus, these very blunt and shallow wedges are spaced $l = 130$ μm apart with an average wedge angle $\alpha = 5$ to 10°. Two hundred of these wedges are spaced on average along the length of the copper surface. The local load on each wedge is $p = P_{nominal}/200$.

During the friction test, the load is first applied before sliding begins. Application of this large load causes the higher asperity peaks from the steel platen to indent the copper surface. As sliding begins the indenting steel wedge causes a ridge of

Table 3 Estimates of the subsurface deformation using slip line theory for a sliding wedge asperity

Wedge slope	Local interface friction, f	Predicted depth of subsurface deformation, μm
5°	0.5	38
10°	0.5	14
5°	0.9	15
10°	0.9	5

Note: Data obtained using the methods of Ref 18-22

Table 4 Estimates of the depth of subsurface deformation using the upper bound approach for a sliding wedge asperity with a wedge slope of 5° and a local friction factor of 0.6

Normal pressure, P MPa	P/σ_0	Predicted depth of subsurface deformation, μm	Average subsurface depth of nanometer spaced lamellar boundaries, μm
12	0.4	6	4.4
17	0.6	9	6.8
22	0.7	11	7.5

Source: Ref 21, 24

copper to develop (Fig. 17(b)). The steel slider is considered to deform elastically while the copper deforms both elastically and plastically. This assumption is reasonable since the surface roughness characteristics of the platen were virtually identical before and after testing, except for some very slight wear mentioned earlier.

4.3.2 Applying Asperity Models to Zone 4

The mechanical interactions between individual surface asperities, the adhesion between asperity junctions, and surface plowing by asperities have been modeled and explored experimentally in many studies (Ref 11-14, 16, 18-22, 24). For light loads, the local surface deformation is confined primarily to the asperities themselves and the extension of this deformation below the asperities remains less than the asperity height. For larger loads, a ridge or standing wave of the softer material is created and propagated by the moving asperities of the harder material and more material below the asperities is engaged in the deformation.

The resistance to sliding and the deformation field caused by the interaction of surface asperities and the propagation of the standing wave or ridge has been calculated using slip line field theory by Wanheim, Bay, Petersen and Abilgaard (Ref 16, 20) and Challen, Oxley and McLean (Ref 18, 22), and using an upper bound approach by Avitzur, Huang, Zhu and Nakamura (Ref 21, 24). These solutions were obtained by assuming a two-dimensional plane strain configuration with elastic perfectly plastic behavior for the case of a steady state wave. The surface deformation fields calculated by these models in general depend on the angle or slope of the asperities (which are idealized as wedges), their spacing, the normal pressure, and the local friction or interfacial strength between the contacting asperity surfaces.

Using the force balance and slip line geometry the depth of surface deformation is determined by the geometry of Challen and Oxley's simplified slip line field diagram and their equations in Ref 18 and 22. The depth of the surface deformation calculated from their model depends on the choice of asperity angle α and the local friction f at the interface. Further, it was assumed in this case that the wave could only develop to a length between asperities of $l = 130$ μm. This range of results (Table 3) shows that the depth of surface deformation increases with decreasing local friction and with decreasing slope or asperity angle α.

A higher value of $f \geq 0.9$ provides the better estimate of surface deformation and also better estimates our high global friction values of μ (Fig. 3a). Values of $f > 0.9$ are required to match our global friction values, which range between 0.6 and 0.8. Note also that a lower value of $f = 0.5$ was found to be more appropriate for oil lubricated surfaces (Ref 22) in contrast to our dry surfaces. The kinematic conditions of the above model would then predict a depth of plastic deformation which is between 5.5 and 15 μm. Those predictions are within a factor of two of the values observed for Zone 4 (Table 2).

Avitzur and Nakamura (Ref 24) have plotted the results of their upper bound analysis in terms of the plastic depth below the surface scaled to the length l between wedges vs a nondimensional normal load $p/\sigma_0 l$ (σ_0 is the bulk yield stress). Since p is the load per unit depth on an individual asperity summit, $p/\sigma_0 l = P_{nomimal}/\sigma_0$. The surface depths versus normal load taken from Fig. 12 of Ref 24 are shown in Table 4 for a slope of $\alpha = 5°$ and a local friction value of 0.6. Although our evidence suggests that a higher local friction factor should be used, those values were not provided in their paper. In using their graph we used the initial yield stress in tension of 30 MPa. Work hardening is not considered. The calculated depth of this plastic deformation (Table 4) is within a factor of two of our data for Zone 4 (Table 2) as well as showing an increase in depth with increasing load.

Both of the above analyses show that the kinematics of the surface asperities and a moving ridge or wave provide a good physical model of a large source of the deformation observed in Zone 4. This fit is quite reasonable considering that the analysis is for an elastic perfectly plastic material, while the real material work hardens tremendously and may not reach a steady state. Also these analyses consider only a single pass of the wedge, whereas in a friction test, many asperities pass over a location in the sample, i.e. 1000, in the present case.

Furthermore, the statistical distributions of asperity height, angle, and length must play some role which neither we, nor these simple models have considered. Work hardening would modify the geometry and flow of the copper ridge or wave with repeated passages of an asperity wedge. Work hardening would also increase the depth of plastic deformation. The increase in depth due to work hardening, however, appears to be less than a factor of two as evidenced by the experiments in Ref 22 performed on a highly work hardening aluminum alloy. Thus, these asperity models explain the deformation in Zone 4, but not the much deeper deformation in Zones 2 and 3.

One further difference with our data and these wave models is the location of the maximum stress and strain. In our data the maximum stress and strain occurs at the surface, whereas in the

wave models it occurs below the surface and at some small distance below the indentation of the ridge into the surface (Ref 20, 22, 23). Thus, there are additional forces affecting Zone 4.

4.3.3 Local Contact of Smooth Bodies

Deformation of two contacting bodies will also be affected by the nominal geometry of contact, such as the contact of two spheres, a cylinder or a sphere on a flat half space, or two flat surfaces as in our case (i.e. Fig. 17(a)). Mechanics solutions for these types of geometries have been steadily extended, from the Hertzian solutions for elastic contact of half spaces to perfectly plastic solutions and to kinematic hardening (for examples see Johnson (Ref 15, 23, 25)). These types of solutions provide estimates of the localized subsurface deformation caused by the nominal geometry. While rough surfaces (asperities) can change the exact stress field caused by the nominal geometry and a superposition of these two effects is not always valid, these two sources for the overall stress field are distinct.

It is thus illustrative to simply consider the nominal case to gain an understanding of the depth range for that nominal field and the size of the strain which develops. In solutions for the stress concentrations due to either the line load of a smooth cylinder or the circular loading of a sphere, the depth of the stress field is three times the half contact width.

The maximum shear stress lies at the surface for friction coefficients greater than 0.33 and below the surface for friction coefficients less than 0.33 (Ref 25). The strains that develop with a single contact are very small, on the order of 0.1% (Ref 25). The large subsurface strains which are observed experimentally are the result of plastic ratcheting of these strains over thousands of contact cycles (Ref 25). In general, the effect of a rough surface would be to widen the nominal area of contact and lower the stresses, thereby increasing the depth of plastic deformation while decreasing its magnitude (Ref 23).

If our geometry fit this type of local loading, then these "Hertzian" contact stresses could explain the depth of deformation in Zones 2 and 3. However, the nominal local contact is two flat surfaces in our experiments. The mechanics for this nominal geometry provides for a constant shear stress across the entire thickness of the sample without generating any local subsurface fields (ignoring the small regions closest to the outer edges of the sample). Thus, this flat nominal geometry is not the source of deformation in Zones 2 and 3.

One could invoke a sample waviness on top of the surface roughness, which would cause a "Hertzian" type loading and thus deeper deformation. While there is probably some waviness in the samples, this waviness could not be frequent enough to provide the number of contacts cycles in which to increase the strains by plastic ratcheting to the large values observed.

4.3.4 The Role of Adhesion

The local friction values required for the asperity models to predict our Zone 4 are high, suggesting that a significant degree of adhesion occurs along the local contact region. This adhesion is further suggested by the film of copper adhering to the platen counterface following a test, and by the removal and reattachment of long strips of the copper surface layers. Local regions of adhesion would create their own stress fields, since local adhesions create cracklike features with a loading similar to a Mode II crack.

Preliminary estimates suggest that the stress field of a Mode II crack extends well beyond the depth of Zone 4 and may be the source of much of the deformation in Zones 2 and 3. The Mode II stress field would also affect Zone 4 by providing the maximum stress concentration at the surface, as is observed in the microstructure. While Mode II cracking in friction has been analyzed for subsurface cracking in the delamination theory of wear (Ref 47, 48), it has not been considered in the present context. The role of the adhesion and Mode II stress fields will be explored in a later paper.

4.3.5 Contributions to the Global Friction Model

None of the above models of friction can provide all of the contributions to the global friction factor that we measure. The asperity models discussed above make a large contribution to that global friction factor. However, to match the non-Coulomb friction behavior and the large dependence of the friction force on normal pressure, other mechanisms need to contribute, including adhesion.

5. Summary and Conclusions

There is a distinct pattern of stress and strain induced microstructures that develop as a result of stress concentrations imposed by sliding. These structures are further modified by deformation-induced temperature increases, and by the repeated shaving off and redeposition of surface layers. These structures provide a quantitative means for estimating the material stress fields and for comparing them with friction models.

It was found that asperity deformation models, which consider a moving wave, can explain one contribution to friction coefficients and the friction induced stress concentrations. However, the microstructural observations also show that another contribution is required to match the friction values and the observed stress and strain fields. It is postulated that local adhesion is another necessary factor.

The observed microstructures reveal the tremendous potential for continued strain hardening of metals during confined deformation. This ability of materials to continue strain hardening beyond our expectations, coupled to the potential for an ever increasing stress field at surface discontinuities, such as an asperity wedge or the root of the notch caused by local adhesion, means that a tremendously hard surface layer evolves during sliding. The evolution of this highly hardened microstructure and the attendant steep gradient in the material flow stress with depth below the surface will cause an evolving friction coefficient and a changing dissipation of friction energy. Thus, these evolving structures need to be incorporated into friction and wear models.

Acknowledgments

The authors would like to thank J. Scola for the preparation of the TEM samples and B. Bernal for help with the SEM. This

work was supported by U.S. DOE under contract No. DE-AC04-94AL85000.

References

1. D.A. Rigney and J.P. Hirth, Plastic Deformation and Sliding Friction of Metals, *Wear*, Vol 53, 1979, p 345-370
2. D. Kuhlmann-Wilsdorf and L.K. Ives, Subsurface Hardening in Erosion-Damaged Copper as Inferred from the Dislocation Cell Structure and Its Dependence on Particle Velocity and Angle of Impact, *Wear*, Vol 85, 1983, p 361-373
3. P. Heilman, W.A.T. Clark, and D.A. Rigney, Orientation Determination of Subsurface Cells Generated by Sliding, *Acta Metall.*, Vol 31, 1983, p 1293-1305
4. D.A. Rigney, M.G.S. Naylor, R. Divakar, and L.K. Ives, Low Energy Structures Caused by Sliding and by Particle Impact, *Mater. Sci. Eng.*, Vol 81, 1986, p 409-425
5. S.L. Rice, H. Nowotny, and S.F. Wayne, A Survey of the Development of Subsurface Zones in the Wear of Materials, *Key Eng. Maters.*, Vol 33, 1989, p 77-100
6. J.J. Wert, The Role of Microstructure Subsurface Damage Induced by Sliding Contact, *Key Eng. Maters.*, Vol 33, 1989, p 101-134
7. Y. Zhu and D. Kuhlmann-Wilsdorf, Determining Subsurface Stress Distributions in Tribological Samples from Dislocation Cell Sizes in Low Energy Dislocation Structures, *Mater. Sci. and Eng.*, Vol A113, 1989, p 297-303
8. S.K. Ganapathi, M. Aindow, H.L. Fraser, and D.A. Rigney, A Comparative Study of the Nanocrystalline Material Produced by Sliding Wear and Inert Gas Condensation, *Mater. Res. Soc. Symp. Proc.*, Vol 206, 1991, p 593-598
9. W.M. Rainforth, R. Stevens, and J. Nutting, Deformation Structures Induced by Sliding Contact, *Phil. Mag. A*, Vol 66, 1992, p 621-641
10. A.J. Perez-Unzueta and J.H. Beynon, Microstructure and Wear Resistance of Pearlitic Rail Steels, *Wear*, Vol 162-164, 1993, p 173-182
11. F.P. Bowden, A.J.W. Moore, and D. Tabor, The Ploughing and Adhesion of Sliding Metals, *J. Appl. Physics*, Vol 14, 1943, p 80-91
12. F.P. Bowden and D. Tabor, *The Friction and Lubrication of Solids*, Oxford Press, 1950
13. A.P. Green, Friction between Unlubricated Metals: A Theoretical Analysis of the Junction Model, *Proc. Roy. Soc. London, A*, Vol 228, 1955, p 191-204
14. D. Tabor, Junction Growth in Metallic Friction: The Role of Combined Stresses and Surface Contamination, *Proc. Roy. Soc. London, A*, Vol 251, 1959, p 378-393
15. J.E. Merwin and K.L. Johnson, An Analysis of Plastic Deformation in Rolling Contact, *Proc. Instit. Mech. Eng.*, Vol 177, 1963, p 676-690
16. N. Bay, T. Wanheim, and A.S. Peteresen, R_a and the Average Effective Strain of Surface Asperities Deformed in Metal Working, *Wear*, Vol 34, 1975, p 77-84
17. N.P. Suh, An Overview of the Delamination Theory of Wear, *Wear*, Vol 44, 1977, p 1-16
18. J.M. Challen and P.L.B. Oxley, An Explanation of the Different Regimes of Friction and Wear Using Asperity Deformation Models, *Wear*, Vol 53, 1979, p 229-243
19. N.P. Suh and H.C. Sin, The Genesis of Friction, *Wear*, Vol 69, 1981, p 91-114
20. T. Abildgaard and T. Wanheim, An Investigation into the Mechanisms of Abrasive Wear and Processing of Materials, *Proc. 2nd Cairo University Mechanical Design and Production Conf.*, 1982, p 521-529
21. B. Avitzur, C.K. Huang, and Y.D. Zhu, A Friction Model Based on the Upper-Bound Approach to the Ridge and Sublayer Deformations, *Wear*, Vol 95, 1984, p 59-77
22. J.M. Challen, L.J. McLean, and P.L.B. Oxley, Plastic Deformation of a Metal Surface in Sliding Contact with a Hard Wedge: Its Relation to Friction and Wear, *Proc. R. London A*, Vol 394, 1984, p 161-181
23. K.L. Johnson, *Contact Mechanics*, Cambridge Univ. Press, 1985
24. B. Avitzur and Y. Nakamura, Analytical Determination of Friction Resistance as a Function of Normal Load and Geometry of Surface Irregularities, *Wear*, Vol 107, 1986, p 367-383
25. K.L. Johnson, The Mechanics of Plastic Deformation of Surface and Subsurface Layers in Rolling and Sliding Contact, *Key Eng. Maters.*, Vol 33, 1989, p 17-34
26. D.B. Dawson, J.S. Korellis, P.S. McCafferty, D.A. Hughes, and L.I. Weingarten, Friction and Near Surface Deformation at Sliding Interfaces, submitted for publication
27. R. Alani and P.R. Swann, Recent Advances in Ion Milling Techniques and Instrumentation for TEM Specimen Preparation of Materials, in *Proceedings of the ACEM-12 and ANZSCB-11 Joint Conference on Electron Microscopy*, Feb 1992, Perth, Australia
28. B. Bay, N. Hansen, D.A. Hughes, and D. Kuhlmann-Wilsdorf, Evolution of fcc Deformation Structures in Polyslip, *Acta Metall. Mater.*, Vol 40, 1992, p 205-219
29. D.A. Hughes and N. Hansen, Microstructural Evolution in Nickel during Rolling to Large Strains, *Metall. Trans. A*, Vol 24A, 1993, p 2021-2037
30. J. Gil Sevillano, P. van Houtte, and E. Aernoudt, Large Strain Work Hardening and Textures, *Prog. Mater. Sci.*, Vol 25, 1981, p 69-412
31. J. Alberdi, "Grandes Deformaciones Plasticas en Frio en Policristales de Cobre y Aluminio (Torsion)," PhD. Thesis, Universidad de Navarra Facultad de Ciencias, San Sebastian, 1984
32. D.A. Hughes and W.D. Nix, Strain Hardening and Substructural Evolution in Ni-Co Solid Solutions at Large Strains, *Mater. Sci. Eng.*, Vol A122, 1989, p 153-172
33. B. Bay, N. Hansen, and D. Kuhlmann-Wilsdorf, Microstructural Evolution in Rolled Aluminum, *Mater. Sci. Eng.*, Vol A158, 1992, p 139-146
34. N. Hansen and D. Juul Jensen, Mechanisms of Deformation, Recovery and Recrystallization of Aluminum, *Hot Deformation of Aluminum Alloys*, T.G. Langdon et al., Ed., TMS, 1991, p 3-19
35. D.A. Hughes and N. Hansen, A Comparison of the Evolution of Cold and Hot Deformation Microstructures and Textures in fcc Metals, *Advances in Hot Deformation Textures and Microstructures*, T. Bieler, K. Bowman, and J.J. Jonas, Ed., TMS, in press, 1994
36. D. Kuhlmann-Wilsdorf, Theory of Plastic Deformation: Properties of Low Energy Dislocation Structures, *Mater. Sci. Eng.*, Vol A133, 1989, p 1-41
37. N. Hansen, Cold Deformed Microstructures, *Mater. Sci. Technol.*, Vol 6, 1990, p 1039-1047
38. B. Bay, N. Hansen, and D. Kuhlmann-Wilsdorf, Deformation Structures in Lightly Rolled Pure Aluminum, *Mater. Sci. Eng.*, Vol A113, 1989, p 385-397
39. D.A. Hughes and N. Hansen, Microstructural Evolution in Nickel during Rolling and Torsion, *Mater. Sci. Technol.*, Vol 7, 1991, p 544-553
40. V.S. Ananthan, T. Leffers, and N. Hansen, Cell and Band Structure in Cold-Rolled Polycrystalline Copper, *Mater. Sci. Technol.*, Vol 7, 1991, p 1069-1075
41. G.I. Taylor, Plastic Strain in Metals, *J. Inst. Met.*, Vol 62, 1938, p 307-324
42. D. Kuhlmann-Wilsdorf and N. Hansen, Geometrically Necessary, Incidental and Subgrain Boundaries, *Scripta Metall. Mater.*, Vol 25, 1991, p 1557-1562

43. R.W.K. Honeycombe, *The Plastic Deformation of Metals*, 2nd ed., Edward Arnold, 1984, p 213

44. G.T. Gray III, P.S. Follansbee, and C.E. Frantz, Effect of Residual Strains on the Substructure Development and Mechanical Response of Shock-Loaded Copper, *Mater. Sci. Engr.*, Vol A111, 1989, p 9-16

45. D. Kuhlmann-Wilsdorf and N. Hansen, Theory of Work Hardening Applied to Stages IV and III, *Metall. Trans. A*, Vol 20, 1989, p 2393-2397

46. U.S. Lindholm, A. Nagy, G.R. Johnson, and J.M. Hoegfeldt, Large Strain, High Strain Rate Testing of Copper, *Trans. ASME J. Eng. Mater. and Tech.*, Vol 102, 1980, p 376-381

47. J.R. Fleming and N.P. Suh, Mechanics of Crack Propagation, *Wear*, Vol 44, 1977, p 39-56

48. D.A. Hills and D.W. Ashelby, On the Determination of Stress Intensification Factors for a Wearing Half Space, *Eng. Fract. Mech.*, Vol 13, 1980, p 69-78